HiSST: 2nd International Conference on
High-Speed Vehicle Science & Technology
11–15 September 2022, Bruges, Belgium

Thermal Effects of Plume Impingement on a Hypersonic Vehicle

Jack Hillyer[1], Luke Doherty[1], David Estruch-Samper[2], James Barth[3], Matthew Mcgilvray[1]

Abstract

The thermal effects of plume impingement on the fuselage of a hypersonic vehicle were investigated using a plume generator mounted to a flat plate model in the Oxford High Density Tunnel at Mach 7. The model was instrumented with thin film heat transfer gauges, pressure transducers, Pressure Sensitive Paint and thermocouples. Schlieren photography was used to visualize the flowfield. Exit Pressure Ratios of up to 22 were tested, with CO_2 as the cold injected gas. Three nozzles were used to explore the effect of changing the expansion profile on heat transfer: a 5 mm conical nozzle, a 6 mm conical nozzle and a 6 mm Rao nozzle. It has shown that initially Stanton number decreases by up to 90% with cold gas injection, but flow separation causes the Stanton number to increase up to 125% of the no injection condition. This significant decrease in heat transfer indicates that there will be direct contact between the rocket engine plume and the fuselage, allowing for significant heat transfer to the fuselage.

Keywords: *Plume impingement, underexpanded jets, shock impingement, Skylon*

Nomenclature

Latin

EPR – Exit Pressure Ratio
GIS – Gas Injection System
HDT – High Density Tunnel
M – Mach number
MAP – Model Alignment Probe
NACA – National Advisory Committee for Aeronautics
PSP – Pressure Sensitive Paint
TFG – Thin Film Gauge
R – Specific gas constant of air
T – Temperature
c – Specific Heat Capacity
p – Static pressure
q – Heat flux
u – Freestream speed
x – Downstream distance from the leading edge of the model

Greek

γ – Ratio of specific heats
μ – Viscosity
ρ – Density

Subscripts

0 – Stagnation
2 – Lower Plenum
∞ – Freestream
w – Wall

1. Introduction

Extremely high aerodynamic heat loads are one of the fundamental difficulties in hypersonic vehicle design [1]. Complex geometries result in shock waves interacting with the boundary layer of the vehicle, causing separation and reattachment of the boundary layer in the vicinity of the shock impingement. Previous studies [2, 3, 4, 5, 6, 7, 8] have shown that this shock boundary layer interaction results in large

[1]*Department of Engineering Science, Parks Road, Oxford, OX1 3PJ corresponding author email address: jack.hillyer@eng.ox.ac.uk*
[2]*Reaction Engines LTD, Culham Science Centre, Abingdon, Oxon, OX14 3DB David.estruch-samper@reactionengines.co.uk*
[3]*Reaction Engines LTD, Culham Science Centre, Abingdon, Oxon, OX14 3DB james.barth@reactionengines.co.uk*

aerodynamic heat loads. In the case of the X-15 [9], shock boundary layer interaction almost led to the loss of the flight vehicle. Additional heating can also arise from the interaction of the engine plume and the vehicle. In the case of rockets, this interaction takes two forms: (1) Base heating of the rocket and (2) highly underexpanded plumes. Base heating refers to the interaction of the underexpanded plumes generated by a rocket with a multiple nozzle configuration. This interaction results in a recirculation region at the base of the vehicle, which leads to a high convective heat load [10, 11, 12, 13, 14]. For highly underexpanded plumes, the Prandtl-Meyer expansion angle can surpass 90 degrees [15], which can lead to the plume wrapping around the sides of the vehicle. Additional heating then results from this direct contact between the combustion products within the plume and the fuselage.

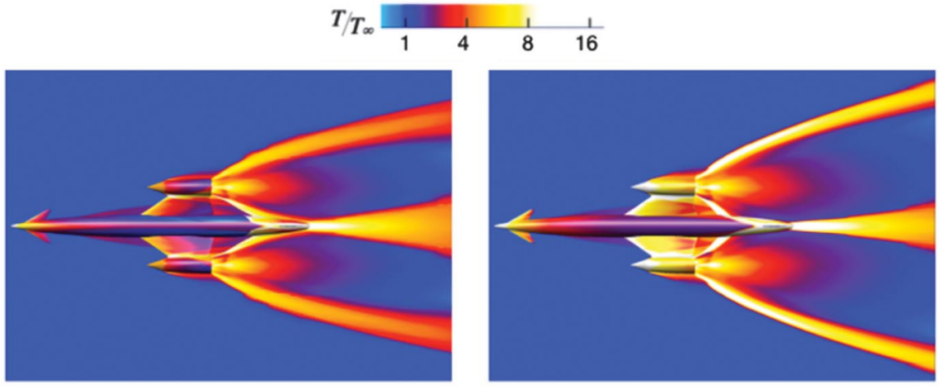

Fig 1. Top down view of the thermal environment around Skylon at Mach 12.189 (left) and Mach 16.969 (right). Adapted from [16].

Skylon is a reusable spaceplane proposed by Reaction Engines Limited (REL) serving as the first stage of a two stage space transportation system. A study performed by Mehta [16] has shown that at moderate and high Mach numbers, the aft fuselage of Skylon is engulfed by the rocket plumes (see Fig. 1). The fuselage is subject to a combined thermal load from the impingement of the plume barrel shock (formed when the edges of the plume overexpand past ambient pressure and then must recompress) and the interaction of the rocket plume itself with the fuselage. This combined thermal load has led to concerns regarding the structural integrity of the fuselage in the plume impingement region. This study investigates the thermal effects of plume impingement on a hypersonic vehicle. It uses a flat plate model instrumented with pressure transducers, thin film heat transfer gauges, Pressure Sensitive Paint and thermocouples. The flowfield is visualized with schlieren photography.

2. Facility

2.1. High Density Tunnel

This experiment was run in the Oxford High Density Tunnel (HDT), a Ludwieg tunnel located in the Osney Thermofluids Institute [17]. It consists of a 17.4 m long, 152 mm internal diameter barrel, separated from the nozzle plenum and free-jet nozzle by an upstream facing plug valve. In this work a Mach 7 contoured nozzle with exit diameter 350 mm was used. The test gas was air and the barrel was electrically heated to 500 K to avoid issues with liquefaction. Full details regarding the test condition are provided in Section 3.1.

A test in HDT is initiated by opening the plug valve. This allows the high pressure, heated gas to expand through the plug valve into the facility plenum, where it stagnates before passing through the facility nozzle. Opening of the plug valve generates an upstream travelling rarefaction wave, which reflects off of the rear facility wall. Steady supply conditions to the facility nozzle are attained until the return of this rarefaction wave to the plug valve, resulting in a drop in supply condition. The rarefaction wave reflects and the process repeats, causing the HDT to produce several steady flow plateaus of up to 35 ms each (see Fig. 7) [18]. A schematic of the facility, showing the expansion waves in the barrel and

the experimental model in the test section is given in Fig. 2.

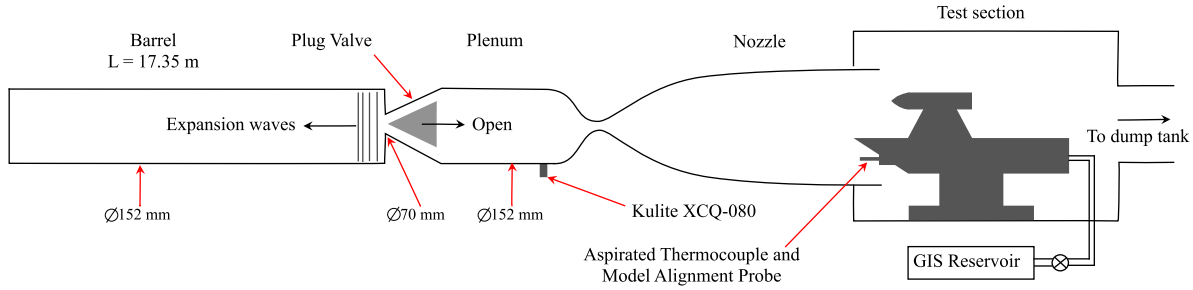

Fig 2. Schematic of the Oxford High Density Tunnel with the model installed in the test section. Adapted from [19]

2.2. The Gas Injection System

The HDT is equipped with a cold Gas Injection System (GIS). The GIS consists of a gas bottle and regulator connected to a reservoir external to the facility test section. The reservoir is separated from the gas line that enters the test section by a fast acting solenoid valve, actuated by an electrical signal sent by the tunnel control system at a prescribed time. This valve controls the flow from the chamber to the model. The GIS reservoir is unheated, and has a maximum pressure rating of 35 bar. The GIS connects to the back of the model, via hosing with an ID of 8 mm.

2.3. Test Condition Monitoring

The facility test condition was monitored using a total temperature probe and a Pitot pressure probe mounted on the underside of the flat plate (see Fig. 3). The total temperature probe consisted of an 0.003" aspirated thermocouple. The aspirated thermocouple has a heating element wound around its mount, heating the thermocouple for the test and reducing its response time. However, the response time is still significant enough that the measured temperature does not represent the actual flow temperature, so processing is required to attain the heat transfer coefficient and half length of the aspirated thermocouple. Knowledge of these properties allows the total temperature trace to be found. The processing is outlined in Hermann [20] and requires a minimum of three tests per tunnel condition (fill pressure and fill temperature), each different initial thermocouple temperatures. The Pitot pressure measurement was measured using a 3.5 bar pressure range Kulite XTL-140 (S)M, mounted in the Model Alignment Probe (MAP) developed by Bustard [21]. The MAP was also used to measure the pitch and yaw of the flat plate, using four Kulite XCL-152-25A, each with a maximum pressure of 172 kPa, arranged at 90° intervals around the probe.

3. Model Design

3.1. Mechanical Design

The experimental model developed for this work is shown in Fig. 3 as a cross section through the vertical symmetry plane. The model consists of six major components: the wing, nose cone, sensor plate, nozzle, lower plenum, and flat plate. All components were manufactured from Aluminium 7075 T6. The nose cone was removable, allowing access to the sensor plate in the upper plenum. The flat plate measured 140 mm wide x 700 mm long, had a wedge angle of 20° and featured a slot for a boundary layer trip. The plume generator consists of an 18° ogive cone with a 50 mm base diameter mounted on a cylinder of 150 mm length. The wing used a NACA 0008 profile, which provided sufficient wall thickness for the four 4.5 mm diameter gas lines between the lower and upper plenum. The internal gas lines had an effective area 25% greater than the cross-sectional area of the GIS pipework. This ensured the injected flow choked at the model nozzle throat, simplifying the analysis.

Three interchangeable nozzles were designed for this experiment, allowing for the effect of nozzle geometry on plume size and heat transfer to be investigated. Each nozzle had an area ratio of 17. Shown in Fig. 4, nozzles A and B were conical nozzles with throat diameters of 5 mm and 6 mm

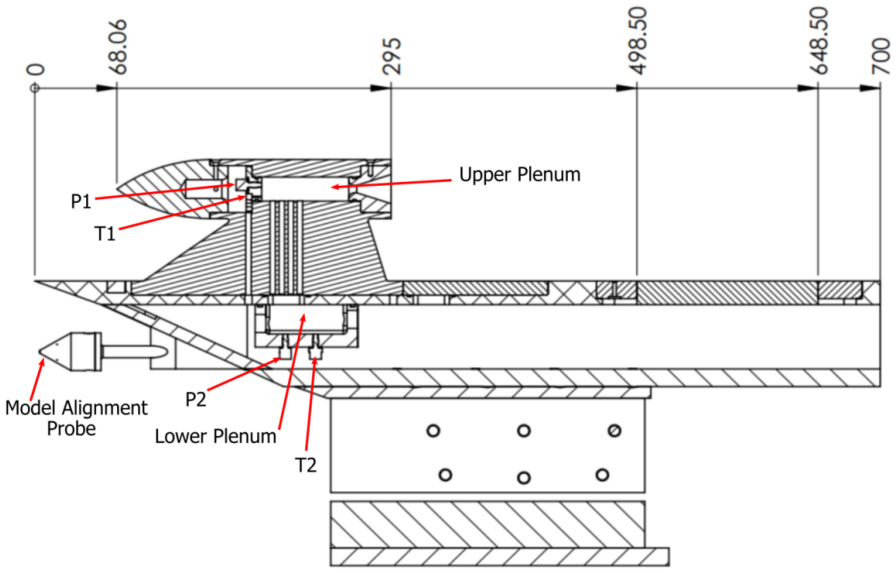

Fig 3. Cross Section of the model

respectively. Nozzle C also had a throat diameter of 6 mm but was a contoured nozzle designed in accordance with Rao [22].

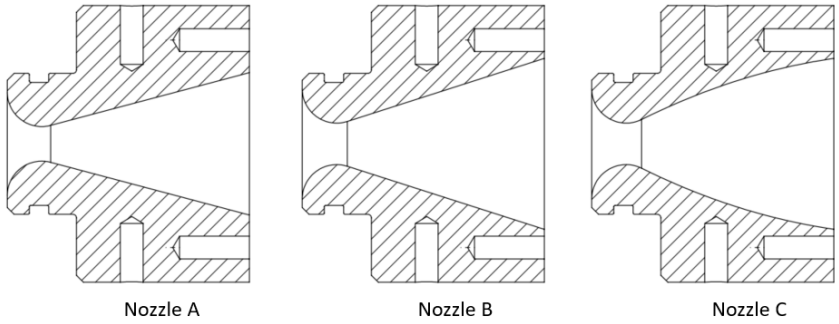

Fig 4. The internal profiles of the 3 nozzles used in this experiment

3.2. Instrumentation

This experiment utilized Thin Film heat transfer Gauges (TFG), pressure transducers, thermocouples, Pressure Sensitive Paint and Schlieren photography. All pressure transducers and thermocouples were recorded at a frequency of 100 kHz on a National Instruments Data Acquisition system, consisting of NI PXIE-6368 cards housed in a NI PXIE-1082 chassis. The TFG data was recorded using an ASH Wireless Electronics AC26-C0006 Lancaster heat transfer amplifier at a frequency of 125 kHz.

3.2.1. Plume Generator

The plume generator featured two plenum chambers, both instrumented for pressure and temperature. The pressure sensors, labelled as P1 and P2 in Fig. 3, were Kulite XT-190 (S)M pressure transducers, with maximum pressures of 35 bar. The temperature sensors, T1 and T2 in Fig. 3, were 0.003" thermocouples, with T2 having identical geometry to a Kulite XT-190. The same geometry was not possible for T1 due to space constraints, so T1 was potted into the sensor plate using epoxy.

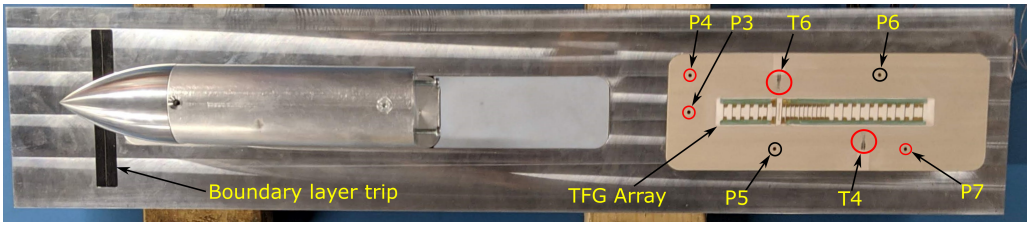

Fig 5. Top down view of the flat plate with the instrumentation annotated. Red circles indicate the sensors that were not operational during the test campaign

3.2.2. Flat Plate

The flat plate is instrumented with five Kulite XT-140M Pressure transducers in the plume impingement region, 2 with a maximum pressure of 0.35 bar and 3 with a maximum pressure of 0.7 bar (see Fig. 5). Additionally, the temperature of the flat plate is measured by two Omega CO2-K thin foil thermocouples.

This experiment utilized Thin Film Gauges (TFG) to measure the heat flux in the plume impingement region. The TFG's used in this experiment are analysed as semi-infinite substrate heat transfer gauges as the short test times of the experiment mean that the conduction can be considered as one-dimensional. The heat transfer data is calculated using the techniques outlined in Collins [23].

The measured heat flux data are presented in the form of the non-dimensional Stanton number averaged over the test time. In Eqn 1, Juliano [24] defines the Stanton number using the freestream stagnation temperature rather than the recovery temperature, noting that for a flat plate at Mach 7, this yields a value approximately 20% greater than that based on the difference between adiabatic wall and recovery temperatures.

$$St = \frac{q}{\rho_\infty u_\infty c_p (T_0 - T_w)} \tag{1}$$

Where St is the Stanton number, q is the heat flux, u_∞ is the speed of the freestream, ρ_∞ is the density of the freestream, c_p is the specific heat capacity of air, T_0 is the total temperature and T_w is the wall temperature of the model. Assuming isentropic flow, the Stanton number is thus given by Eqn 2. It should be noted that no boundary layer edge values are needed to be calculated using this definition, simplifying the data reduction.

$$St = \frac{q\sqrt{\frac{RT_0}{1+\frac{1}{2}(\gamma-1)M^2}}}{p_\infty M c_p \sqrt{\gamma}(T_0 - T_w)} \tag{2}$$

Where R is the specific gas constant for air, γ is the ratio of specific heats, p_∞ is the static pressure of the freestream, and M is the Mach number of the freestream.

3.2.3. Flowfield Visualisation

Schlieren photography was also used to visualize the flowfield. 300 mm diameter, 1660 mm focal length mirrors were used in a z type setup, with a horizontal knife edge and illumination being provided by a green Luminus CBT-180 LED. The Schlieren was recorded on a Photron Fastcam Mini AX200 at 6400 fps and an exposure of 83 µs.

Pressure Sensitive Paint (PSP) was sprayed on one half of the flat plate, starting at a downstream location from the leading edge of 425 mm and extending to the trailing edge of the plate. The PSP was illuminated by a Luminus CBT-120 UV LED and its response was recorded on a Photron Mini UX100 camera at 2000fps and an exposure of 125 µs. Due to a lack of optical access from the top of the test

section, a mirror was used to image the PSP onto the camera (shown in Fig 6). The data was processed using techniques detailed in [25], with a spatial average near to a pressure sensor (P6 in Fig 5) being equated to the pressure measured by that transducer.

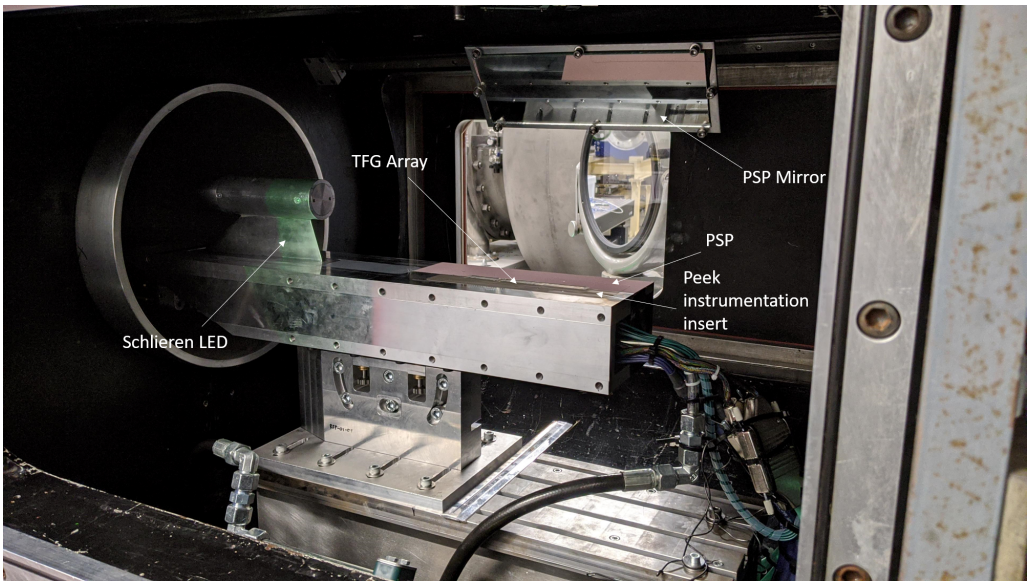

Fig 6. The model in the test section

4. Results

4.1. Test Conditions

Table 1 shows the average freestream conditions attained on the 2nd steady pressure plateau, calculated using pressure readings from HDT's nozzle plenum and isentropic flow relations. All testing was conducted at the same freestream condition, with model nozzle and injection pressure being varied between tests. Additionally, for shots 838 and 842, the experimental model was moved downstream by 75 mm and the flat plate was rotated 90 degrees. This led to the facility nozzle shock impinging upon the flat plate at x = 625 mm, so data for x > 625 mm is not presented. For shot 842, the plume generator was removed and the model was run in a flat plate configuration.

Table 1. Nominal test conditions

Mach Number	P_∞ (Pa)	T_0	ρ_∞ (g/m^3)	u (m/s)	μ_∞ (Pas)	$Re_{unit}(10^6/m)$
7	406	450	25.7	945.4	3.3 $\times 10^{-6}$	7.3

Table 2. Injection Conditions

HDT Shot No.	Nozzle	P_2 (bar)	T_2 (K)	EPR
823	5mm Conical	8.80	291.9	10.6
825	5mm Conical	0	291.9	0
829	5mm Conical	18.4	291.8	22.0
830	6mm Conical	15.0	290.8	17.7
834	6mm Rao	8.8	291.3	18.0
838	5mm Conical	0	293.3	0
842	N/A	N/A	N/A	N/A

Table 2 gives the different injection conditions between tests. During testing, the pressure transducer within the upper plenum of the model was broken, so pressure data from the transducer within the lower plenum is presented. Numerical simulations have shown that the pressure in the lower plenum is within 10% of the pressure in the upper plenum. Also given in Table 2 is the Exit Pressure Ratio (EPR), defined as the ratio between the static pressure of the plume at nozzle exit and the freestream static pressure, which governs the size and shape of the plume [26].

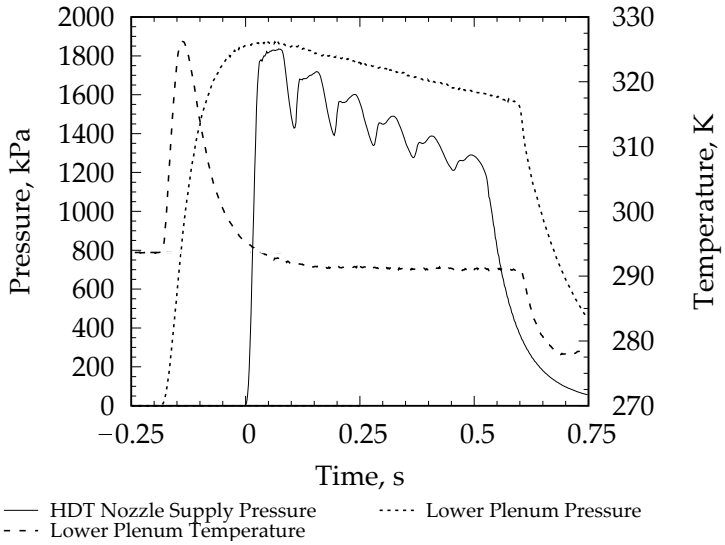

Fig 7. Graph showing the HDT nozzle supply pressure vs engine pressure and temperature

4.2. PSP Response

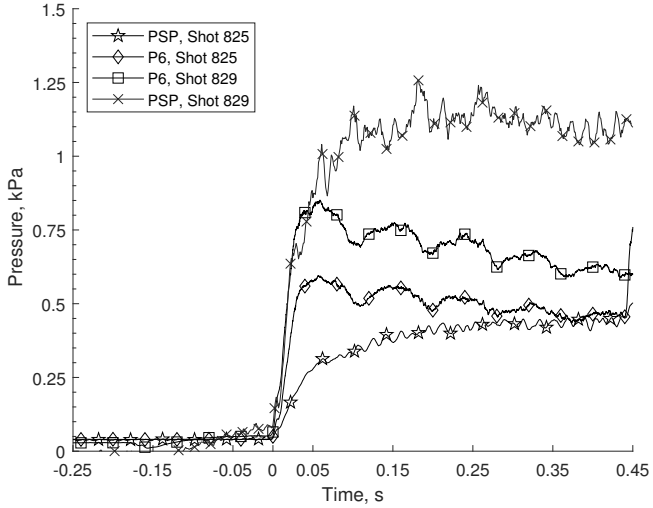

Fig 8. Comparison of the response of the PSP and reference kulite, P6, with (shot 829) and without (shot 825) injection

Fig. 8 shows a comparison between the PSP signal and the reference Kulite signal. It can be seen that the PSP exhibits a fast rise time, but does not track the reference Kulite signal accurately. It can also be seen that the PSP underpredicts the pressure in the no injection case, but over-predicts the pressure when injection is present. From this, it can be assumed that the CO_2 is having an effect on the PSP that is not captured in the calibration. As a result, the PSP presented in this paper can be used for

qualitative results only, and will be presented as variations of intensity, with lower levels of intensity being associated with regions of higher pressure.

In addition to this, the PSP in Fig. 11 and Fig 14 exhibits a diagonal line between 525 mm $<$ x $<$ 575mm. This is a result of damage during install and is not a physical effect.

4.3. Flat Plate Configuration

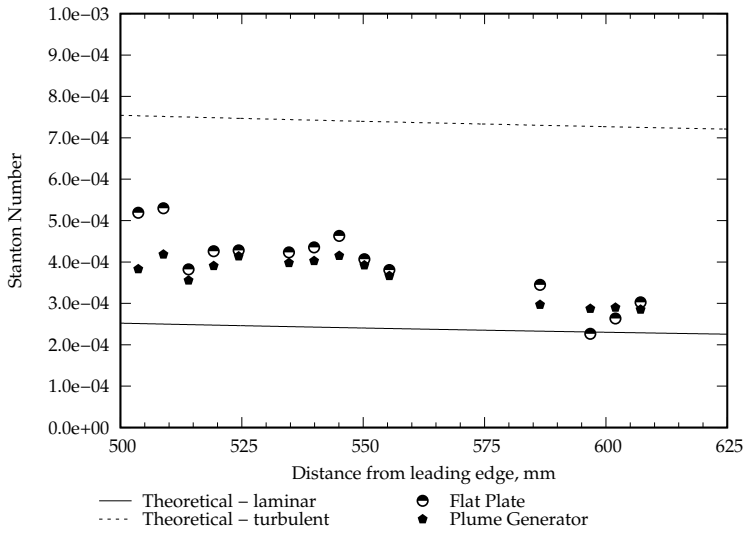

Fig 9. Comparison of the heat transfer measured with and without the plume generator in place

Fig. 9 shows the heat transfer measured from shot 842 compared to theoretical values for turbulent and laminar boundary layers. The theoretical Stanton number was computed using the relations described in Crabtree [27], which uses the Eckert reference enthalpy method. It can be seen from this that the boundary layer likely remains laminar for the length of the flat plate.

4.4. Flat Plate with Plume Generator

There are three shocks present in the Schlieren in Fig. 9. The first shock is the facility nozzle shock, indicating that the model was too large and causing blockage. The second shock, originating at approximately x = 295 mm, is the reflection of the leading edge shock formed by the engine. This separates the boundary layer. The third shock, originating at approximately x = 390 mm, is the reattachment shock. The heat transfer data shown in Fig. 9 indicates that this separation and reattachment of the boundary layer did not cause transition.

4.5. Effect of injection

As can be seen from fig. 7, the plume generator fires approximately 250 ms before the tunnel, meaning the plume expands into the evacuated test section and impinges upon the flat plate. The arrival of the freestream pushes the attachment point of the plume downstream. The lower the EPR, the further the attachment point gets pushed back. This can be inferred from the barrel shocks visible in the schlieren in Fig. 10, where it can be seen that the angle of the lower barrel shock is less steep for the lower EPR case. However, in all cases the attachment point remains upstream of the TFG array. In addition to pushing the attachment point downstream, the freestream also compresses the plume. This causes the width of the plume to decrease, with lower EPR's being compressed more and becoming thinner. This is evidenced by the areas of low intensity in the PSP, shown in Fig. 11, where it can be seen that the plume with an EPR of 10.6 is much thinner than the plume with an EPR of 22. The PSP upstream of plume impingement indicates the degree of mixing between the freestream and the plume - the greater the intensity change, the more blockage created by the plume and thus less mixing between the flows. From this, it can be seen that increasing EPR decreases the amount of mixing between the freestream and the plume.

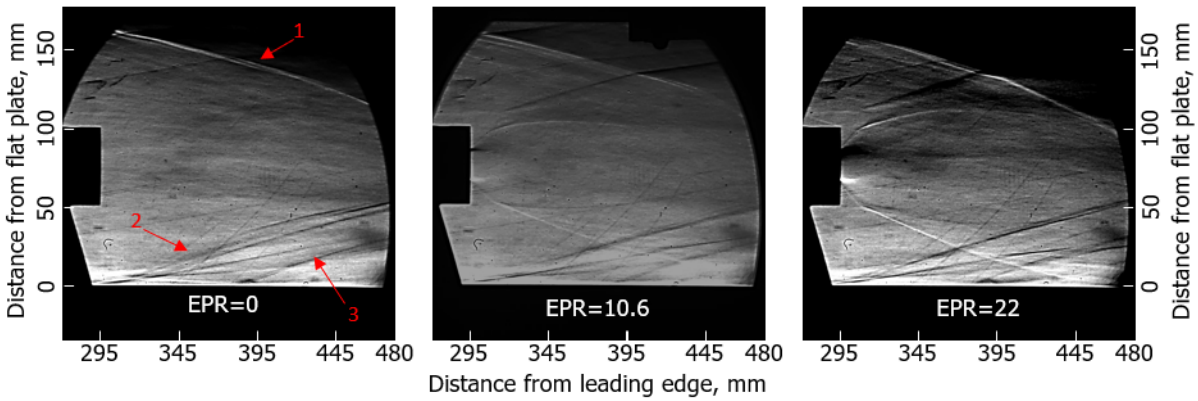

Fig 10. Schlieren of the flowfield with EPR varied. Left to right: Shot 825, Shot 823, Shot 829

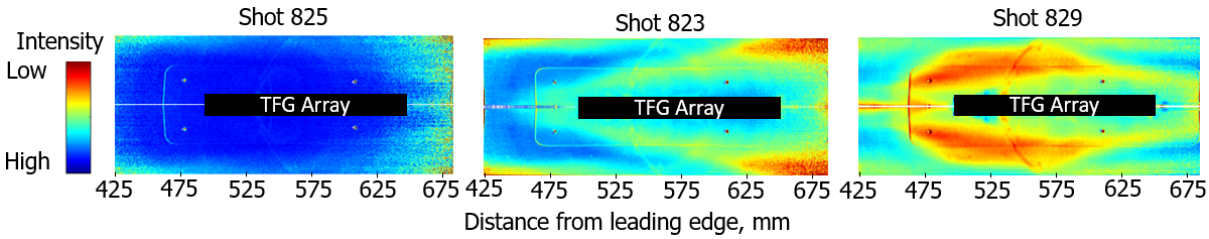

Fig 11. PSP with EPR varied. Left to Right: Shot 825 (EPR=0), Shot 823 (EPR=10.6), Shot 829 (EPR=22). PSP reflected along vertical symmetry plane for clarity.

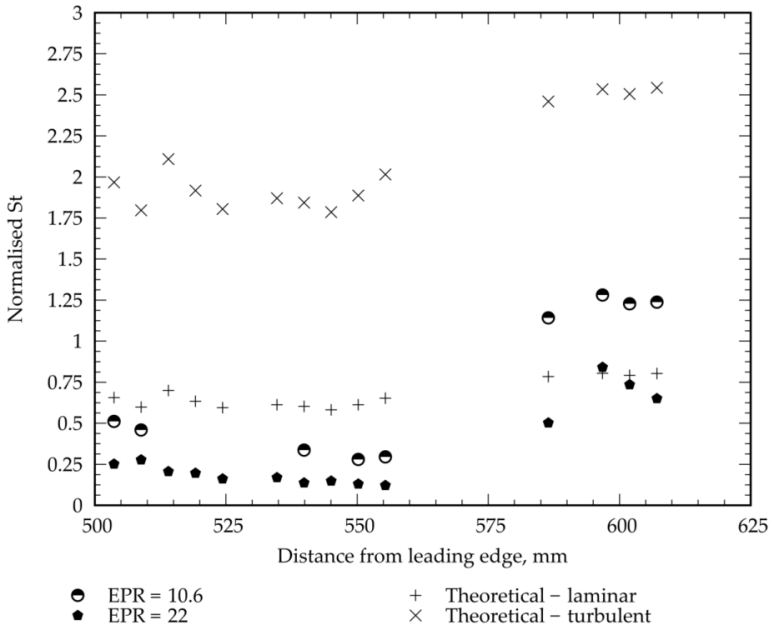

Fig 12. Stanton number normalised by the no injection case (shot 838) for variation in EPR

Fig. 12 shows the variation in heat transfer with different EPR's. It can be seen that for $500 < x < 555$ mm there is significant cooling when the plume generator is on, with Stanton number being reduced by up to 70% and 85% relative to the no injection case for EPR's of 10.6 and 22, respectively. This

cooling is a result of the presence of cold CO_2 from the plume, with greater cooling indicating greater CO_2 presence. This shows that increasing the EPR increases the amount of CO_2 on the plate.

It can also be seen that there is a rise in heat transfer for x > 585 mm, with heat transfer increasing to 85% of the no injection case for EPR = 22, and to 125% of the injection case for the EPR of 10.6 case. This is a result of flow separation caused the barrel shock leaving the plate. This is evidenced in the PSP of shot 829, where the barrel shock footprint, indicated by red areas in the PSP, decreases in size at approximately that location. This was confirmed in Schlieren when the Schlieren setup was moved downstream, but it is not presented as it this Schlieren was performed at different freestream conditions and so does not form part of a consistent data set. The magnitude of the heat transfer increase is greater for the lower EPR case, indicating that the smaller plume induces a larger separation region.

4.6. Effect of changing nozzle geometry

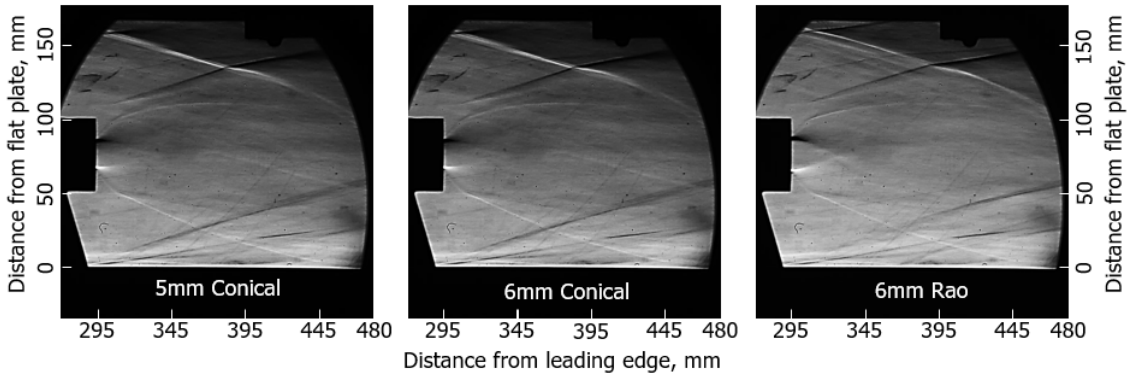

Fig 13. Schlieren of the flowfield with model nozzle varied. Left to right: Shot 829, Shot 830, Shot 834

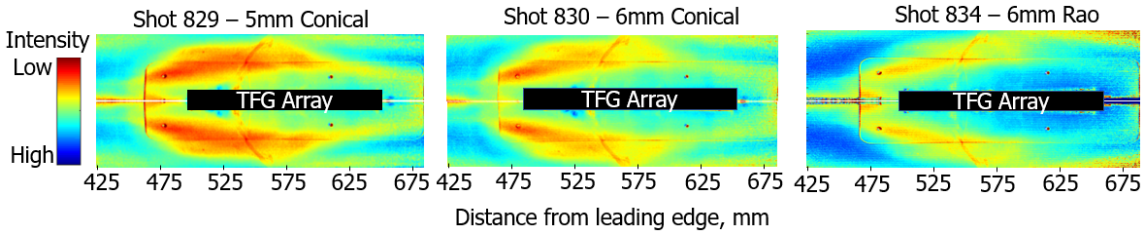

Fig 14. PSP with model nozzle varied. Left to right: Shot 829 (5 mm conical), Shot 830 (6 mm conical), Shot 834 (6 mm Rao). PSP reflected along vertical symmetry plane for clarity.

The PSP in Fig. 14 shows that the footprint of the plumes produced by each nozzle are consistent. The main variation in the PSP is the magnitude of intensity change in the barrel shock impingement region, with greater intensity change indicating a stronger barrel shock. From this, it can be inferred that the 5mm conical nozzle produces the strongest barrel shock, a consequence of the greater EPR attained by this nozzle, whilst the Rao nozzle produces the weakest barrel shock. The Schlieren of the 6mm Rao nozzle plume, shown in Fig. 13, exhibits a diamond-shaped flow structure that is not present in the Schlieren of the 6mm conical nozzle. This indicates the flow leaving the Rao nozzle is more parallel to the cylinder axis than the streamlines leaving the 6mm conical nozzle. Consequently, the plume overexpands past the freestream pressure less for the Rao nozzle, producing a weaker barrel shock.

The strength of each nozzles' barrel shock is further evidenced in the PSP upstream of the barrel shock footprint, where the pattern is repeated. As discussed in Section 4.5, greater intensity change upstream of the barrel shock impingement is indicative of less mixing between the plume and the freestream, and

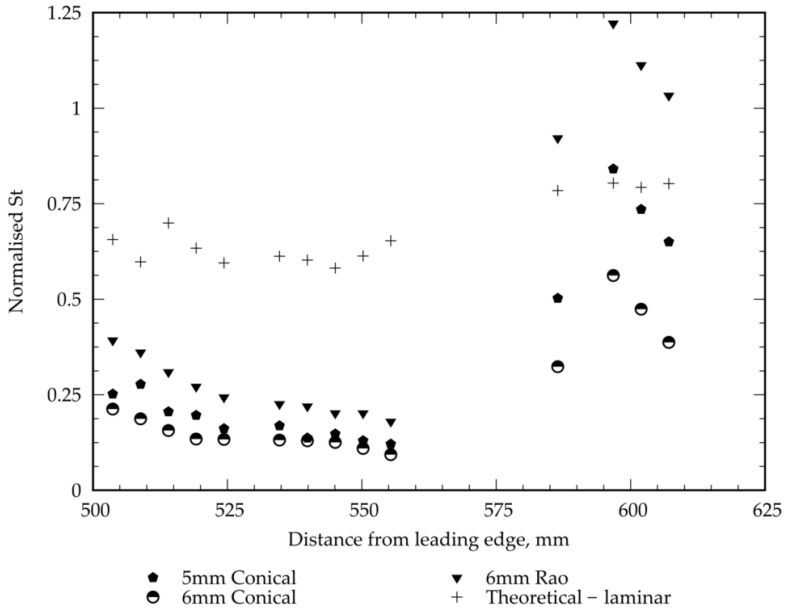

Fig 15. Stanton number normalised by the no injection case (shot 838) for nozzle variation

thus a stronger barrel shock.

The TFG data shown in Fig. 15 again shows significant cooling for $500 < x < 555$ mm, with reductions in heat transfer of up to 85%, 90% and 80% relative to the no injection case for the 5mm conical, 6mm conical and 6 mm Rao nozzle, respectively. The 6mm Rao nozzle exhibiting the least cooling indicates the greatest mixing between the plume and freestream, which is in agreement with the PSP data discussed above. However, the TFG data shows that the 5mm conical nozzle resulted in less cooling than the 6mm conical nozzle, despite the decreased mixing. This is likely a consequence of the lower exit area of the 5mm conical nozzle, which creates a smaller plume and thus decreases the CO_2 presence on the TFG array.

The TFG data in Fig. 15 also shows that there is a rise in heat transfer for all 3 nozzles for $x > 575$ mm. As discussed in section 4.5, this is a result of the plume separating from the flat plate, with greater heat transfer indicating a larger separation region. The Rao nozzle increases the Stanton number to up to 120%, the 5mm conical up to 85% and the 6mm conical up to 55% of the no injection case. From this, it can be seen that the Rao nozzle produces the largest separation region, followed by the 5mm conical nozzle and finally the 6mm conical nozzle.

5. Conclusions

This project utilised a plume generator mounted to a flat plate to determine the effects of plume impingement. It has provided experimental data for the Stanton number on a flat plate with a cold gas plume impinging upon it. It has shown that initially Stanton number decreases by up to 90% with cold gas injection, but flow separation causes the Stanton number to increase up to 125% of the no injection condition. This significant decrease in heat transfer indicates that there will be direct contact between the rocket engine plume and the fuselage, allowing for significant heat transfer. Further work could include heating of the injected gas so that the ratio of the total temperature of the injected gas to the freestream can be matched to that of flight.

6. Acknowledgements

The authors would like to thank Reaction Engines for sponsoring this work. Additionally, many thanks to the Oxford Thermofluid Institute technicians and TPB Precision Engineering for manufacture of the experimental model, and to Joseph Steer for his rigorous operation of the HDT during this campaign.

References

[1] Anderson, J.D.: Hypersonic and high temperature gas dynamics. Aiaa (2000)

[2] Marvin, J., Horstman, C., Rubesin, M., Coakley, T., Kussoy, M.: An experimental and numerical investigation of shock-wave induced turbulent boundary-layer separation at hypersonic speeds. Aerodynamic Analyses Requiring Advanced Computers, Pt. 1 (1975)

[3] Erdem, E., Kontis, K., Johnstone, E., Murray, N., Steelant, J.: Experiments on transitional shock wave–boundary layer interactions at Mach 5. Experiments in fluids, 54(10):1–22 (2013)

[4] Babinsky, H., Harvey, J.K.: Shock wave-boundary-layer interactions, vol. 32. Cambridge University Press (2011)

[5] Bernardini, M., Asproulias, I., Larsson, J., Pirozzoli, S., Grasso, F.: Heat transfer and wall temperature effects in shock wave turbulent boundary layer interactions. Physical Review Fluids, 1(8):084403 (2016)

[6] Xiao, F., Li, Z., Zhang, Z., Zhu, Y., Yang, J.: Hypersonic shock wave interactions on a V-shaped blunt leading edge. AIAA Journal, 56(1):356–367 (2018)

[7] Back, L.H., Cuffel, R.F.: Shock wave/turbulent boundary-layer interactions with and without surface cooling. AIAA Journal, 14(4):526–532 (1976)

[8] Alzner, E., Zakkay, V.: Turbulent boundary-layer shock interaction with and without injection. AIAA Journal, 9(9):1769–1776 (1971)

[9] Watts, J.D.: Flight experience with shock impingement and interference heating on the X-15-2 research airplane. NASA TM X-1669 (1968)

[10] Mehta, M., Dufrene, A.T., Seaford, M., Knox, K.: Space Launch System Base Heating Test: Environments and Base Flow Physics. 54th AIAA Aerospace Sciences Meeting, p. 0547 (2016)

[11] Dufrene, A.T., Mehta, M., MacLean, M.G., Seaford, M., Holden, M.S.: Space Launch System Base Heating Test: Experimental Operations and Results. 54th AIAA Aerospace Sciences Meeting, p. 0546 (2016)

[12] Brewer, E.B.: Experimental investigation of base flow field at high altitude for a four-engine clustered nozzle configuration. National Aeronautics and Space Administration (1969)

[13] Patel, D.: Antares liquid rocket engine convective base heating: AJ-26 to RD-181. AIAA Modeling and Simulation Technologies Conference, p. 4415 (2016)

[14] Payne, R.G., Jones, I.P.: Summary of Saturn I base thermal environment. Journal of Spacecraft and Rockets, 3(4):489–497 (1966)

[15] John, D.A., Anderson, D.: Modern compressible flow (2003)

[16] Mehta, U., Aftosmis, M., Bowles, J., Pandya, S.: Skylon aerospace plane and its aerodynamics and plumes. Journal of Spacecraft and Rockets, 53(2):340–353 (2016)

[17] McGilvray, M., Doherty, L.J., Neely, A.J., Pearce, R., Ireland, P.: The Oxford High Density Tunnel. 20th AIAA international space planes and hypersonic systems and technologies conference, p. 3548 (2015)

[18] Wylie, S., Doherty, L., McGilvray, M.: Commissioning of the Oxford High Density Tunnel (HDT) for boundary layer instability measurements at Mach 7. 2018 Fluid Dynamics Conference, p. 3074 (2018)

[19] Hillyer, J., Doherty, L., Hambidge, C., McGilvray, M.: Extension of test time in Ludwieg Tunnels. Second international conference on flight vehicles, aerothermodynamics and re-entry missions and engineering, Heilbronn, Germany (2022)

[20] Hermann, T., McGilvray, M., Hambidge, C., Doherty, L., Buttsworth, D.: Total temperature measurements in the Oxford High Density Tunnel. International conference on flight vehicles, aerothermodynamics and re-entry missions and engineering, FAR, Monopoli, Italy (2019)

[21] Doherty, L., Bustard, A.: The Development of a Model-Alignment Probe for the Oxford High Density Tunnel (2019)

[22] Rao, G.: Exhaust nozzle contour for optimum thrust. Journal of Jet Propulsion, 28(6):377–382 (1958)

[23] Collins, M., Chana, K., Povey, T.: New technique for the fabrication of miniature thin film heat flux gauges. Measurement science and technology, 26(2):025303 (2015)

[24] Juliano, T.J., Jewell, J.S., Kimmel, R.L.: HIFiRE-5b boundary-layer transition length and turbulent overshoot. Journal of Spacecraft and Rockets, 58(2):265–283 (2021)

[25] Hermann, T., Ifti, H., McGilvray, M., Doherty, L., Geraets, R.: Mixing characteristics in a hypersonic flow around a transpiration cooled flat plate model (2018)

[26] Goethert, B., Barnes, L.: Some studies of the flow pattern at the base of missiles with rocket exhaust jets. Tech. rep., ARO INC ARNOLD AFS TN (1960)

[27] Crabtree, L., Dommett, R., Woodley, J.: Estimation of heat transfer to flat plates, cones and blunt bodies (1965)